Release and fate of As mobilized via bio-oxidation of arsenopyrite in acid mine drainage: Importance of As/Fe/S speciation and As(III) immobilization

Chen, H-R., Zhang, D-R., Li, Q., Nie, Z. & Pakostova, E

DOI 10.1016/j.watres.2022.118957
ISSN 0043-1354

Publisher: Elsevier

Release and fate of As mobilized via bio-oxidation of arsenopyrite in acid mine drainage: Importance of As/Fe/S speciation and As(III) immobilization

Hong-Rui Chen[a], Duo-Rui Zhang[a,*], Qian Li[a,*], Zhen-yuan Nie[a], Eva Pakostova[b]

[a] School of Minerals Processing and Bioengineering, Central South University, Changsha 410083, China

[b] Centre for Sport, Exercise and Life Sciences, Coventry University, Coventry, CV1 5FB, UK

*Correspondence to be addressed: e-mail: drzhang@csu.edu.cn; csuliqian208018@csu.edu.cn

Abstract:

Mining activities expose sulfidic minerals including arsenopyrite (FeAsS) to acid mine drainage (AMD). The subsequent release of toxic arsenic (As) can have great negative implications for the environment and human health. This study investigated the evolution of secondary products and As speciation transformations during arsenopyrite bio-oxidation in AMD collected from a polymetallic mine. Immobilization of the As solubilized via arsenopyrite bio-oxidation using red mud (RM) was also studied. The results show that the high ionic strength (concentrations of dissolved Fe^{3+}, SO_4^{2-}, and Ca^{2+} reached values up to 0.75, 3.38, and 0.35 g/L, respectively) and redox potential (up to +621 mV) of AMD (caused primarily by Fe^{3+}) enhanced the dissolution of arsenopyrite. A high $[Fe]_{aq}/[As]_{aq}$ ratio in the AMD favored the precipitation of tooeleite during arsenopyrite bio-oxidation, and the formation of other poorly crystalline products such as schwertmannite and amorphous ferric arsenate also contributed to As immobilization. Bacterial cells served as important nucleation sites for the precipitation of mineral phases. Arsenopyrite completely dissolved after 12 days of bio-oxidation in AMD and the $[As]_{aq}$ (mainly present as As(III)) reached 1.92 g/L, while a greater $[As]_{aq}$ was observed in a basal salts medium (BSM) assay (reaching 3.02 g/L). An RM addition significantly promoted As(III) immobilization, with final $[As(III)]_{aq}$ decreasing to 0.16 and 1.43 g/L in AMD and BSM assays respectively. No oxidation of As(III) was detected during the immobilization process. These findings can help predict As release from arsenopyrite on contact with AMD and, on a broader scale, assist in designing remediation and treatment strategies to mitigate As contamination in mining.

Key words: Arsenic; Arsenopyrite bio-oxidation; Speciation; Acid mine drainage; Arsenic immobilization; Red mud

1. Introduction

Arsenic (As) pollution in groundwater, surface waters and soils can have serious negative effects on human health (Hong et al., 2021). Arsenic pollution is caused both by natural geomicrobiological processes and anthropogenic activities such as pesticide application, landfill pile leaching and mining (Guo et al., 2013; Matschullat, 2000). The latter is considered a primary source of As pollution in natural environments (Tabelin et al., 2021). Extraction and processing of valuable metals such as gold and copper lead to an elevated exposure of As-bearing sulfide minerals (ABSMs) (e.g., arsenopyrite (FeAsS) and enargite (Cu_3AsS_4)) to water and oxygen. Oxidation of ABSMs results in a release of As into the environment. Iron- and/or sulfur-oxidizing microorganisms (ISOMs) significantly enhance the rates of oxidation of sulfidic minerals (including ABSMs), thus promoting the generation of acid mine drainage (AMD) (Corkhill et al., 2008).

Several studies have investigated the mechanisms of the oxidation of arsenopyrite (which is the most abundant ABSM in many ore deposits), including the effects of the following environmental factors: oxygen (Walker et al., 2006), pH (Yu et al., 2007), oxidants and/or metal oxides (including H_2O_2 (Ma et al., 2016), Fe^{3+} (Neil and Jun, 2016), MnO_2 and Fe_2O_3 (Liu et al., 2015)), anions (Cl^- (Zheng et al., 2020), PO_4^{3-} (Park et al., 2020) and HCO_3^- (Wu et al., 2020)), and organic matter (humic and fulvic acids

(Wu et al., 2019)). However, most of the previously reported works were performed under laboratory conditions (in deionized water containing different effectors, with the solution pH adjusted using diluted H_2SO_4, HCl, HNO_3 or NaOH) and a very limited number of studies have systematically investigated the oxidation behavior of arsenopyrite mediated by acidophilic ISOMs and the subsequent release of As from the mineral in natural AMD.

During arsenopyrite bio-oxidation, the oxidation of As proceeds in a series of one-electron transfers in which As(III) and As(V) are the dominant As species (Murciego et al., 2019). The products of bio-oxidation of iron (Fe) and sulfur (S) in arsenopyrite, Fe^{3+} and SO_4^{2-}, promote the formation of various secondary products such as jarosites ($MFe_3(SO_4)_2(OH)_6$, where M is a monovalent cation, such as NH_4^+, K^+ or H_3O^+), schwertmannite ($Fe_8O_8(OH)_{8-2x}(SO_4)_x$ where $1 \leq x \leq 1.75$), elemental sulfur (S^0), amorphous ferric arsenate (FA), and scorodite ($FeAsO_4 \cdot 2H_2O$) (Corkhill and Vaughan, 2009). The formation and transformations of these mineral phases are strongly affected by physicochemical parameters (pH, redox potential (ORP), metal ions, Fe/As and As/S ratios etc.) as well as the composition and activity of microbial communities. As could be expected, the above factors can also significantly affect the mobility and fate of As. Most laboratory experiments are performed in culture media (e.g., basal salts (BSM), 9K, MAC, MSM), while the arsenopyrite bio-oxidation in AMD can be expected to be a significantly more complex process. A high ORP and elevated concentrations of sulfate and metal(loid)s (such as Fe, Al, Zn) in AMD (Cheng et al., 2009) can significantly affect the growth of bacteria, dissolution of arsenopyrite, physicochemical

properties of secondary products, and thus also the transport and fate of As. For example, a higher Fe/Al molar ratio in As-rich AMD was reported to promote As immobilization (Adra et al., 2016; Yuan et al., 2021).

In-situ immobilization of As released via arsenopyrite bio-oxidation is a key step in controlling As pollution in mine-impacted environments. As(III) is significantly more toxic to biological systems than As(V) (Boussouga et al., 2021), and can be immobilized using Fe(III) and Al(III) oxides via adsorption, efficiency of which depends greatly on the ionic strength and pH (Wei et al., 2019). By-products generated by the secondary Al industry have shown a great potential in metal(loid) removal; red mud (RM) can regulate arsenopyrite dissolution and the fate of As during bio-oxidation through changes in solution parameters such as pH, As speciation, and oxidation properties of biogenic Fe/S intermediates and products (Zhang et al., 2021). Consequently, Fe(III) and protons (H^+) generated during Fe and S bio-oxidation play a key role in the transformations of RM. Zhang et al. (2022) reported that bacterially generated Fe(III) improved the As(V) adsorption capacity of Fe(III)/Al(III) (hydr)oxides formed, while no As(III) immobilization was observed. Our knowledge is limited about the roles of RM in the immobilization of As (particularly As(III)) during arsenopyrite bio-oxidation in AMD and the feasibility of using RM as a stabilizing agent of As-bearing mine wastes remains unknown.

Mining activities that generate AMD as well as expose sulfidic minerals to the atmosphere inadvertently lead to an intensified contact of arsenopyrite with AMD, which can cause serious As contamination of waters and soils in the mining area (Park

et al., 2019). A better understanding is needed of the release and subsequent fate of As mobilized via bio-oxidation of arsenopyrite on contact with AMD, since the composition of AMD (particularly, high ORP and elevated concentrations of dissolved ions such as SO_4^{2-} and Fe^{3+}) can greatly affect As mobilization. In this study, bio-oxidation of arsenopyrite and transport of As in natural AMD originating in a polymetallic mine in China were investigated. Differences between the arsenopyrite bio-oxidation in AMD and BSM were studies, with a focus on solution chemistry, morphology and composition of secondary precipitates, and As speciation. Furthermore, the effects of RM on the immobilization of As(III) released via bio-oxidation of arsenopyrite were evaluated. The results of this work advance our understanding of the generation of As-contaminated AMD via bio-oxidation of ABSMs in mine wastes. On a broader scale, the findings provide information that could be useful in waste management, specifically in applications using industrial by-products to treat As-polluted mine wastes.

2. Materials and methods

2.1. Materials

Arsenopyrite used in this study was collected from a Carlin-type gold deposit in the Guangxi province, China. The arsenopyrite sample was ground and sieved to select a particle size of 38 to 75 μm. The elemental composition of the arsenopyrite was 44.91% As, 33.30% Fe, 18.54% S, with minor amounts of Si (1.02%), Al (0.59%), Cu (0.47%), and Ca (0.28%). The morphology of the arsenopyrite was determined using X-ray

diffraction (XRD; D8 ADVANCE, Bruker, Germany) and the mineralogy using field-emission scanning electron microscopy (FE-SEM; TESCAN MIRA3, Czech Republic) (Fig. S1). The RM sample used for immobilization of the As released via arsenopyrite bio-oxidation was obtained from the Aluminum Corporation of China, Jiaozuo, Henan, China. The elemental composition of RM was determined using X-ray fluorescence spectroscopy (XRF, Axios mAX, Netherlands) and the results are shown in Table S1.

The AMD sample used in this work was collected from the Dabaoshan Mine area (24°34'28"N, 113°43'42"), which is the largest polymetallic mine in South China (Chen et al., 2015; Bao et al., 2018). The pH and ORP values of the AMD were 2.04 and +621 mV, respectively. The main elements in the AMD, analyzed using inductively coupled plasma atomic emission spectrometer (ICP-AES, ICPE-9820, Shimadzu Corporation, Japan), comprised (in mg/L): Fe, 751.6; Al, 449.4; Zn, 246.9; Mg, 884.9; Ca, 354.3; Mn, 95; Si, 39.3; Cu, 35.5; Na, 3.0; Cd, 0.792; As, 0.028.

2.2. Bacterial strain and cultivation conditions

Sulfobacillus (S.) thermosulfidooxidans strain YN-22 (accession number of 16S rRNA gene in GenBank: DQ650351) was obtained from the Key Laboratory of Biometallurgy of Ministry of Education of China (Changsha, China). To adapt the strain to arsenopyrite, 10 g/L of the mineral was added to a basal salts medium (BSM) containing (in g/L): $(NH_4)_2SO_4$, 3.0; $MgSO_4$, 0.5; K_2HPO_4, 0.5; KCl, 0.1; $Ca(NO_3)_2$, 0.01.The initial pH of the medium was adjusted to 2.0 ± 0.05 using 5 M H_2SO_4.

2.3. Bio-oxidation of arsenopyrite

Two sets of bioassays were designed to investigate oxidative dissolution of arsenopyrite and the fate of the As released during the bio-oxidation process. The first set was carried out in 250 mL Erlenmeyer flasks containing 10 g/L arsenopyrite in 100 mL AMD that was prior to use sterilized by filtration (0.22 μm). Strain YN-22 was inoculated at initial concentration of 6×10^7 cells/mL. An un-inoculated flask served as an abiotic control. The second set of bioassays was performed as described above, but contained 100 mL of sterile BSM (pH 2.0 ± 0.05, adjusted with 5 M H_2SO_4) instead of AMD.

2.4. Immobilization of As released via arsenopyrite bio-oxidation

For As immobilization experiments, 4 or 8 g/L of RM were added to the biotic systems after 10 days of arsenopyrite bio-oxidation (during which most arsenopyrite was dissolved and significant amounts of As were released into the solution). All assays were prepared in triplicate and incubated at 37 ℃ and 170 rpm. The pH and ORP values in suspension were regularly measured and liquid samples were collected and filtered (0.22 μm) prior to chemical analyses. Solid samples were washed thoroughly with deionized water and dried for 48 h in a vacuum drying oven at 37 ℃, then stored in air-tight containers until further analysis.

2.5. Analytical methods

The concentrations of dissolved total Fe ($[Fe^T]_{aq}$) and ferric iron ($[Fe^{3+}]_{aq}$) were

measured using the colorimetric 5-sulfosalicylic acid spectrophotometry method at 500 nm (UV-2550, SHIMADZU, Japan) (Karamanev et al., 2002). Total As concentration in aqueous samples ($[As^T]_{aq}$) was analyzed by inductively coupled plasma-mass spectrometry (ICP-MS; 7700x, Agilent Technologies, USA) and As speciation ($[As(III)]_{aq}$ and $[As(V)]_{aq}$) was analyzed using high-performance liquid chromatography combined with ICP-MS (HPLC-ICP-MS) with an anion exchange column. Other soluble elements were determined by ICP-AES.

Surface morphology and elemental composition of solid samples were characterized by FE-SEM coupled with an energy-dispersive spectrophotometry (EDS; Hitachi S-4800, Hitachi, Ltd., Japan). Transmission electron microscope (TEM) images were obtained using a Titan G2 60-300 instrument with an energy-dispersive X-ray (EDX) spectrometer and a Tecnai G2 F20 field high-resolution TEM (HRTEM). The mineralogical composition was determined by XRD and analyzed using the mineral liberation analysis (MLA). The MLA data were recorded using a FEI Quanta 650 MLA-FEG field emission scanning electron microscope equipped with two Bruker Quantax X-Flash 5010 EDX detectors. Based on the combined information from backscattered electron (BSE) images and EDX spectra, MLA identified individual grains of different minerals in selected samples (Fandrich et al., 2007). The valence states of As and Fe were determined by X-ray photoelectron spectroscopy (XPS; K-Alpha 1063, Thermo Fisher Scientific, USA), using Al Kα X-ray as an excitation source.

The speciation transformations of As and S in solid samples were characterized by As and S K-edge X-ray absorption near edge structure (XANES) spectroscopy at the

Beijing Synchrotron Radiation Facility (BSRF; Beijing, China). The S K-edge XANES analysis of samples was conducted on 4B7A beamline, together with the analysis of S-bearing reference standards including arsenopyrite, S^0, sodium thiosulfate, jarosite, schwertmannite, tooeleite ($Fe_6(AsO_3)_4(SO_4)(OH)_4 \cdot 4H_2O$), aluminum sulfate, and calcium sulfate. The samples were recorded in the fluorescence mode at ambient temperatures and were scanned at a step width of 0.2 eV from 2445 to 2530 eV. The As K-edge XANES analysis was conducted on 1W2B beamline using a Si (111) double-crystal monochromator. The spectra of samples and As-bearing references (i.e., arsenopyrite, amorphous FA, scorodite, tooeleite, sodium arsenate (Na_3AsO_3), and disodium hydrogen arsenate (Na_2HAsO_4)) were recorded in the transmission mode using a standard 25% Ar-filled ionization chamber, and collected from 11,800 to 11,940 eV, with a step of 0.45 eV and a dwell time of 2 s. Athena software within the Demeter suite of programs was used for the edge-normalization of the Fe/As K-edge XANES spectra and linear combination fitting (LCF) analysis. The goodness of fit parameters were evaluated by the reduced chi-square value (Ravel and Newville, 2005; Datta et al., 2012).

3. Results and discussion

3.1. Kinetics of arsenopyrite bio-oxidation

Compared to the BSM assay, the bio-oxidation of arsenopyrite in AMD was expected to be more complex due to the elevated dissolved metal concentrations (e.g., $[Fe^{3+}]_{aq} > 0.7$ g/L) and high ORP (> +600 mV) of the AMD. In both cases, changes in

the solution parameters including ORP, pH, cell density, [Fe^T], [Fe^{3+}], [As^T], [As(III)], [SO_4^{2-}], and concentrations of other elements such as Al, Si, K, Na, Ca, Mn, Cu, and Zn were investigated.

The ORP value (Fig. 1a) in the AMD systems was affected predominantly by $[Fe^{3+}]_{aq}/[Fe^{2+}]_{aq}$ (Fig. 1c shows changes in $[Fe^T]_{aq}$ and $[Fe^{3+}]_{aq}$) (Zhang et al., 2015) and it sharply decreased from +621 mV to +378 mV after 1 day of arsenopyrite bio-oxidation. This can be explained by the high concentration of Fe^{3+} in the AMD and its reduction to Fe^{2+} on reaction with arsenopyrite, following Eq. 1 (Mckibben et al., 2008). In the BSM assay, the ORP value gradually increased with the initial rapid bio-oxidation of arsenopyrite (first 2 days), followed by a decrease due to an increase in $[Fe^{2+}]_{aq}$ (Fig. 1c). After the ORP reached a maximum value on day 8, a slight decrease followed due to the formation of Fe(III) minerals (which was verified by XRD (results shown in Fig. 4) and XANES (Figs. 8 and 9)). Fig. 1c shows that at a later stage the dissolved Fe in both AMD and BSM biotic assays existed mainly as Fe^{3+}. In AMD, $[Fe^T]_{aq}$ reached 1.53 g/L on day 10, which was a significantly higher value than in BSM (reaching 0.48 g/L on day 10). The continuous increase in both [Fe^T] and [Fe^{3+}] in the AMD system indicated that the dissolution of arsenopyrite and bio-oxidation of Fe^{2+} were ongoing until the end of the experiment.

The initial rapid increase in pH (Fig 1a) in both AMD and BSM assays was caused predominantly by rapid bio-oxidation of Fe^{2+} to Fe^{3+} (Eq. 2). The formation of secondary products such as jarosites (Eq. 3) and ferric arsenate (Eq. 4), and bio-oxidation of S (Eq. 5) are H^+-generating reactions that caused a gradual decrease in the

solution pH after day 2 (Fig. 1a).

$$FeAsS + 5Fe^{3+} + 3H_2O \rightarrow 6Fe^{2+} + H_3AsO_3 + S + 3H^+ \quad (1)$$

$$4Fe^{2+} + 4H^+ + O_2 \xrightarrow{\text{bacteria}} 4Fe^{3+} + 2H_2O \quad (2)$$

$$3Fe^{3+} + 2{SO_4}^{2-} + M^+ + 6H_2O \rightarrow MFe_3(SO_4)_2(OH)_6 + 6H^+ \quad (3)$$

$$H_3AsO_4 + Fe^{3+} \rightarrow FeAsO_4 + 3H^+ \quad (4)$$

$$2S + 3O_2 + 2H_2O \rightarrow 2{SO_4}^{2-} + 4H^+ \quad (5)$$

Fig. 1b shows that the high metal content in AMD negatively affected the growth of *S. thermosulfidooxidans* in the first 2 days, compared to minimal medium. The maximum cell density in the AMD reached 2.1×10^8 cells/mL on day 4, followed by a slight decrease. The cell density in the AMD system was greater at the later stage of arsenopyrite bio-oxidation than that in the BSM assay. Generally, the release of the electron donor Fe^{2+} and accumulation of toxic As are two main factors that affect (the first positively and the latter negatively) bacterial growth and Fe oxidation during arsenopyrite bio-oxidation. High $[As^T]_{aq}$ (Fig. 1d) and a formation of a passivation layer (shown in Fig. 3a, b) inhibited the dissolution of arsenopyrite, which explains the decrease in the cell density (particularly in the BSM assay, after 2 days of bio-oxidation). The relatively low rates of Fe^{2+} oxidation by *S. thermosulfidooxidans* in the first 2 days were ascribed to the inhibitory effects of the elevated concentrations of dissolved metals (in AMD assay) and As released via arsenopyrite oxidative dissolution (in both biotic assays), while from day 2 to 6, the rate of Fe oxidation was higher in AMD (Fig. 1c).

Fig. 1d-f shows that $[As^T]_{aq}$ and $[SO_4^{2-}]_{aq}$ gradually increased as the bio-oxidation of arsenopyrite progressed. An elevated $[As^T]_{aq}$ was detected in the AMD assay in the

initial stage of the experiment, indicating enhanced arsenopyrite dissolution due to a rapid attack of the Fe^{3+} present in AMD on the mineral surface. Importantly, in both AMD and BSM, the solubilized As occurred mainly as As(III) (Fig. 1d). From day 2, $[As^T]_{aq}$ and $[As(III)]_{aq}$ in the AMD assay were noticeably lower than those in BSM assay. This was ascribed to the formation of As(III)-bearing precipitates (e.g., tooeleite, as shown in Figs. 4 and 7). Of note, an obvious decrease in the concentration of Al(III) was found at the initial stage during arsenopyrite bio-oxidation in the AMD assay (Fig. 1e). Previous studies have reported that Al(III) can contribute to As removal via the formation of Al(III)-Fe(III) hydroxides and Al-sulfoxyhydroxide (e.g., basaluminite) (Wang et al., 2019; Igarashi et al., 2020). No significant changes were observed throughout the time course of the experiment in the concentrations of other elements in either of the two assays.

In the AMD sterile control, the ORP value quickly dropped from +618 to +322 mV due to rapid Fe^{3+} reduction on contact with arsenopyrite (Eq. 1), and then it marginally increased over time to +336 mV (Fig. 2a). In the abiotic BSM assay, ORP increased slightly over time, reaching a maximum of +328 mV on day 10, a value significantly lower than the value detected in the corresponding bio-assay (+536 mV). The pH in both abiotic assays did not significantly change during chemical dissolution of arsenopyrite (Fig. 2a). Soluble Fe existed predominantly as Fe^{2+} in both systems (Fig. 2b). The As released from arsenopyrite in sterile AMD water was mainly As(III), while it occurred predominantly as As(V) in the sterile medium (Fig. 2c). In summary, significantly lower arsenopyrite dissolution rates were observed in the abiotic systems

(Fig. 2) compared to the corresponding bio-assays inoculated with *S. thermosulfidooxidans* (Fig. 1).

3.2. Elemental and mineralogical composition of arsenopyrite oxidation products

To describe the surface structure of arsenopyrite residues and oxidation layers formed on the mineral surfaces, and to analyze differences between solids from AMD and BSM assays, the leaching residues were investigated by SEM-EDS. Figs. 3a and S2a show SEM images of amorphous products that formed in large amounts within 2 days of bio-oxidation of arsenopyrite in AMD. These products were composed predominantly of Fe, As, S and O, and attached to the surface of both arsenopyrite and bacterial cells. In comparison, the surface morphology of the bio-oxidized arsenopyrite residue collected from the BSM assay after 2 days (Fig. 3b) differed from that of the AMD residue, showing a fine and dense surface layer enriched in As, S, Fe and O, with a minor amount of K (Fig. S2b). Meanwhile, many bacterial cells were found attached to the mineral surfaces (Fig. S3). After 10 days of bio-oxidation, the arsenopyrite completely dissolved in the AMD biotic system and the typical structure corresponding to the mineral was not identified in the SEM images, but an amorphous precipitate that included bacterial cells occurred (Fig. 3d). In the BSM assay, a well-crystallized passivation layer comprising aggregated disk-like microstructures (with a diameter of ~1 μm) covered the mineral surface (Fig. 3e), and an elevated content of K (besides Fe, S, and O; Fig. S4) implies that it was composed mainly of K-jarosite ($KFe_3(SO_4)_2(OH)_6$), an Fe(III)-oxysulphoxyhydroxide known to incorporate As

(Savage et al., 2005; Zhang et al., 2020). The surface of the arsenopyrite in the BSM sterile control remained intact after 10 days (Fig. 3c), and only a low quantity of oxidation products was formed on the mineral surface in the AMD control system (Fig. 3f).

The XRD results (Fig. 4) show that the phase composition of the bio-oxidized arsenopyrite residue from the AMD system was more complex compared to the residue from BSM. Compared to the arsenopyrite residue collected from the BSM biotic system (shown in Fig. 4b), a greater amount of S^0 and a lower quantity of crystalline jarosite were detected on the surface of the AMD arsenopyrite residue after 2 days of arsenopyrite bio-oxidation. Interestingly, a significant amount of As(III)-bearing precipitate, i.e., tooeleite, was also detected (Fig. 4a) on the AMD residue surface. Tooeleite has previously been identified as a material potentially suitable for As(III) immobilization (Morin et al., 2003). The formation of tooeleite (Eq. 6) is affected primarily by the Fe/As ratio, pH and $[SO_4^{2-}]_{aq}$ (Chai et al., 2016; Nishimura and Robins, 2008). The low solution pH (Fig. 1a) and elevated concentrations of Fe^{3+} (affecting the Fe/As ratio) (Fig. 1c) and SO_4^{2-} (Fig. 1e) in AMD facilitated the enhanced accumulation of tooeleite during arsenopyrite bio-oxidation in this study. This also explains the lower $[As^T]_{aq}$ and $[As(III)]_{aq}$ detected in the AMD system compared to those in BSM (in Fig. 1d). After 10 days of bio-oxidation in AMD, the arsenopyrite almost disappeared and the solid phase comprised mainly tooeleite and S^0, with minor amounts of jarosites, goethite (α-FeOOH), and biotite ($KFeMg_2(AlSi_3O_{10})(OH)_2$) (Fig. 4a). In contrast, the solids collected from BSM after 10 days (Fig. 4b) were composed mainly of jarosites

(which are considered the main components of passivation layers on sulfide surfaces in ore bioleaching; Larsson et al., 1990), S^0, and minor amounts of tooeleite and arsenopyrite. No significant changes were detected in the arsenopyrite in the sterile controls (Fig. 4c), besides a greater amount of S^0 detected in the AMD residue compared to the BSM one.

$$6Fe^{3+} + 4H_3AsO_3 + {SO_4}^{2-} + 8H_2O \rightarrow Fe_6(AsO_3)_4(SO_4)(OH)_4 \cdot 4H_2O + 16H^+ \quad (6)$$

The MLA analysis results (Fig. S5, Table S2) show that in the AMD biotic assay, the content of tooeleite reached 72.02% after 10 days of arsenopyrite bio-oxidation, which was much higher than the tooeleite content in the BSM biotic assay (18.58%), while the contents of jarosites (6.39%) and arsenopyrite (2.14%) in the AMD assay were much lower than those in BSM (62.44 and 10.56%, respectively).

3.3. Speciation transformations of As, Fe, and S during arsenopyrite bio-oxidation

To identify As species in oxidation layers, the arsenopyrite residues from AMD and BSM assays were examined by XPS at different reaction times. The spectra of $As3d_{(5/2)}$ are shown in Fig. 5 (and corresponding fitting parameters are summarized in Table S3). The As species on the surface of arsenopyrite during bio-oxidation in both AMD and BSM were mainly As(-I)-S (41.1 eV), As(0) (41.8 eV), As(I)-O (43.5 eV), As(III)-O (44.35 eV), and As(V)-O (45.25 eV). In comparison to the original arsenopyrite (Fig. 5i), the intensities of As(-I)-S and As(0) peaks decreased and those of As(III)-O and As(V)-O increased due to arsenopyrite bio-oxidation (Fig. 5a,d), and these trends gradually continued as the bio-oxidation process progressed (Fig. 5b,c,e,f).

In the AMD system (Fig. 5a-c), the peak of As(-I)-S for arsenopyrite disappeared after 10 days and As(III)-O became a dominant As species in the oxidation layer (reaching 43.9%) (Fig. 5c), corresponding to the accumulation of tooeleite (Fig. 3). In the BSM assay, the percentage of As(V)-O (46.6%) was greater than that of As(III)-O (34.9%), likely due to an increased formation of As(V)-bearing minerals such as amorphous ferric arsenate and scorodite. These findings are consistent with the results of XANES analysis, described below (Fig. 6).

The As K-edge XANES analysis was performed to further evaluate As speciation during arsenopyrite bio-oxidation (Fig. 6). The XANES spectra of As-bearing references are shown in Fig. 6a. Linear combination fitting (LCF) plots of XANES spectra for the arsenopyrite residues bio-oxidized in AMD and BSM for 10 days are shown in Fig. 6b (dotted lines), closely corresponding to the measured XANES spectra of the bio-oxidized arsenopyrite residues (solid lines). Based on the edge energies, As(III) (11,871.3 eV) dominated in the bio-oxidized residue obtained from the AMD system, while As(V) (11,875 eV) was dominant in the bio-oxidized arsenopyrite residue in the BSM assay.

The LCF results show that As in the arsenopyrite residue collected from the BSM assay after 10 days of bio-oxidation comprised of 48.4% amorphous FA, 21.3% scorodite, 15.6% tooeleite, 8.9% disodium hydrogen arsenate (Na_2HAsO_4), and 5.8% arsenopyrite (Fig. 6c). In contrast, the composition of the bio-oxidized residue from the AMD system was 70.1% tooeleite, 17.5% amorphous FA, and 12.4% Na_3AsO_3, while no arsenopyrite and scorodite were detected (Fig. 6d). Due to its high stability, scorodite

is considered a suitable material for the immobilization and long-term storage of arsenate (Vega-Hernandez et al., 2019). The As released from arsenopyrite at the early stage of bio-oxidation was mainly As(III), which quickly reacted with Fe^{3+} and SO_4^{2-} in AMD to form tooeleite. These results demonstrate that Fe^{3+} cannot efficiently promote the oxidation of As(III) to As(V) in AMD, even at the high concentrations, indicating that the fate of As released from arsenopyrite in AMD significantly differs from that of As mobilized in the BSM assay.

To investigate S speciation in the solid residues after arsenopyrite bio-oxidation, the S K-edge XANES analysis and LCF were performed (Fig. 7). A comparison with the spectra of S-bearing references (Fig. 7a) showed that while a decrease in the intensity of the peak for arsenopyrite (2,471.8 eV) occurred, the intensity of the peaks for S^0 (2,472.6 eV) and SO_4^{2-} (2,482.8 eV) increased gradually during arsenopyrite bio-oxidation in both AMD and BSM systems (Fig. 7b).

The LCF results (Fig. 7c, d) show that the S species in the arsenopyrite residue after 2 days of bio-oxidation in AMD were composed of 40.3% arsenopyrite, 27% S^0, 14.1% jarosites, 9.4% schwertmannite, and 9.2% tooeleite, compared to 57.5% arsenopyrite, 21.7% S^0, 15.6% jarosites, and 5.2% schwertmannite in the BSM residue. After 10 days of bio-oxidation, the S species were tooeleite (37.8%), S^0 (30.6%), schwertmannite (16.7%), and jarosites (14.9%) in the solids from AMD, and 48.2% jarosites, 24.3% S^0, 11.9% arsenopyrite, and minor amounts of schwertmannite (9%) and tooeleite (6.6%) in the BSM residue. These results demonstrate that arsenopyrite bio-oxidation was enhanced in the AMD water. Simultaneously, an increased formation

of schwertmannite (a poorly crystalline Fe(III)-oxyhydroxy sulfate mineral with a tunnel structure and strong binding affinity for metal(loid)s) could facilitate (partial) immobilization of As under acidic conditions through adsorption or co-precipitation reactions, as described by Burton et al. (2009).

A mechanism of arsenopyrite bio-oxidation in AMD is proposed (Fig. 8) based on the above results. Fe^{3+} present in AMD attacks the surface of arsenopyrite. The Fe^{2+} generated via Fe^{3+} reduction and arsenopyrite dissolution serves as an electron donor to chemolithotrophic bacteria, and the extracellular polymeric substances (EPSs) that coat bacterial cells can serve as nucleation sites for precipitation of Fe- or As-bearing products (Wang et al., 2020; Bond et al., 2000). Dissolution of arsenopyrite and efficient bio-oxidation of Fe^{2+} and S result in elevated $[As(III)]_{aq}$, $[Fe^{3+}]_{aq}$ and $[SO_4^{2-}]$ in AMD, promoting the formation of amorphous As(III)/Fe(III) sulfate oxy-hydroxide minerals (e.g., tooeleite and schwertmannite). The elevated formation of the above secondary minerals facilitate As immobilization (particularly that of As(III)) via co-precipitation and/or adsorption (Egal et al., 2009; Duquesne et al., 2003). In comparison to AMD, a greater proportion of As released through bio-oxidation of arsenopyrite in the BSM remains in solution (mainly as As(III)). Importantly, the formation of a dense passivation layer (composed mainly of jarosites, S^0, amorphous FA, and scorodite) on the surface of arsenopyrite in the BSM can limit the attack of Fe^{3+} on the mineral surface and mitigate the release of Fe^{2+} that would support the growth of chemolithotrophs, thus inhibiting the dissolution of arsenopyrite.

3.4. Evaluation of RM for in-situ As immobilization

3.4.1. Effects of RM on AMD enriched with As mobilized via arsenopyrite bio-oxidation

As shown above, elevated concentration of dissolved As (predominantly as As(III)) were detected in AMD due to arsenopyrite bio-oxidation (Fig. 1c, d), which together with the low pH of AMD (< 2.0; Fig. 1a), presents a serious risk for the environment and human health. To investigate the potential of RM to serve as an As adsorbent, small amounts (4 and 8 g/L) of alkaline RM were added to the AMD and BSM assays after 10 days of arsenopyrite bio-oxidation.

Fig. 9a illustrates that the additions of RM to the AMD biotic systems resulted in a significant ORP decrease and pH increase, caused mainly by neutralization reactions and adsorption of Fe^{3+} onto solid surfaces. Four days after the addition of 4 and 8 g/L RM (i.e., on day 14), pH in the assays increased from 1.87 to 2.43 and 3.52 respectively, and ORP decreased from +578 mV to +445 and +315 mV respectively. Similar trends were observed in the BSM assay (Fig. 9c). Fig. 9b shows that the concentration of dissolved As significantly decreased in the AMD systems four days after RM additions, and the murky yellow color of both solutions (with 4 and 8 g/L RM) cleared up after standing for 24 h. Interestingly, the amount of Fe precipitated (similarly to As) correlated with the amount of RM added (Fig. 9b), indicating that Fe^{3+} may play an important role in the As immobilization process. Meanwhile, partial dissolution of RM caused by H^+ and Fe^{3+} attack (Zhang et al., 2022) resulted in the release of low amounts of Al, Si, Ca, and Na into solution (Fig. 9b). The $[As(III)]_{aq}$ decreased from 1.92 g/L to 0.68 and 0.16 g/L in the AMD assays with 4 and 8 g/L RM, respectively (Fig. 9b), while

in the BSM assay with 8 g/L RM, the $[As(III)]_{aq}$ remained high (1.43 g/L) after 4 days of reaction (Fig. 9d). A slight increase in SO_4^{2-} in both AMD and BSM was attributed to bio-oxidation of S^0 and/or dissolution of jarosites (as discussed below and shown in Fig. 14). In the abiotic assays, an increase in pH and decrease in ORP values occurred after 4 and 8 g/L RM were added, and no visible decrease in $[As]_{aq}$ and $[Fe]_{aq}$ was observed (Fig. S6).

3.4.2. Effects of RM on solid products of arsenopyrite bio-oxidation

The SEM results show the morphology of the residue collected from the AMD assay four days after the addition of 4 g/L RM (Fig. 10a, b). The morphology, comprising structures of aggregated nano-sized crystallites, was similar to that of the arsenopyrite residue before RM addition (shown in Fig. 3d), but a low amount of gypsum ($CaSO_4 \cdot 2H_2O$) was present (Fig. 10a). The predominance of As, Fe, S, and O (Fig. 10c) implies that the residue after RM addition was composed mainly of tooeleite, which was also indicated by XRD results shown in Fig. 11a. When 8 g/L RM was added to the AMD bio-oxidation assays, more gypsum was formed and the solid precipitates together with bacterial cells accumulated as nanoscale spheroids (diameter 100-300 nm) (Fig. 10d, e). In contrast, the main solid structures in the BSM after the addition of 8 g/L RM were residual RM and undissolved arsenopyrite covered with a fine passivation layer (Fig. S7).

The XRD results (Fig. 11) indicate that the residue collected from the AMD system four days after the addition of 4 g/L RM was composed of amorphous tooeleite, S^0, and gypsum, with minor amounts of other phases such as ettringite

($Ca_6Al_2(SO_4)_3(OH)_{12}\cdot 26H_2O$), jarosites, and biotite ($KFeMg_2(AlSi_3O_{10})(OH)_2$) (Fig. 11a). Additionally, the two broad peaks in the XRD pattern of the precipitate indicate that the analyzed solids contained substances with poor crystallinity. Interestingly, a small amount of pharmacosiderite ($KFe_4(AsO_4)_3(OH)_4\cdot 6\text{-}7H_2O$) was detected in the assay with 4 g/L RM. Pharmacosiderite has a similar composition to scorodite and its formation has been linked to As and Fe redox reactions associated with microbial activity (Koo et al., 2022). Compared to the residue from the AMD system with 4 g/L RM, the XRD pattern of the solid residue collected from the AMD assay with 8 g/L RM showed more prominent gypsum peaks while jarosite peaks became negligible (Fig. 11b). Small amounts of muscovite ($KAl_2Si_3AlO_{10}(OH)_2$) and hematite (Fe_2O_3) were also detected in the residue. The residue collected from BSM with 8 g/L RM was composed of gypsum and S^0, with minor amounts of tooeleite and arsenopyrite. The intensity of the jarosite peaks decreased after the addition of RM (Fig. S8). Additionally, the higher pH (pH > 4) (Fig. 9c) and lower $[Fe^{3+}]_{aq}$ (Fig. 9d) in the BSM assay (compared to AMD) resulted in a greater abundance of RM components, e.g., muscovite, hematite, kaolinite ($Al_2Si_2O_5(OH)_4$), perovskite ($CaTiO_3$), and diaspore (β-AlO(OH)).

The results of the TEM analysis (Fig. 12) show that the surface of the residue from the AMD assay before RM addition comprised an amorphous layer among needle-like microstructures (Fig. 12a). Four days after 8 g/L RM were added, the amorphous layer covering cell surfaces became denser and thicker, with elevated distributions of As, Al, Si, and O (Fig. 12d), compared to the element distribution before RM was added (Fig.

12c). The corresponding EDS results (Fig. S9, Table S4) indicate that the oxidation layer formed on the cell surfaces before RM was added was comprised mainly of tooeleite. In addition, the decrease in the Fe/As ratio from 1.57 to 1.46 implies that dissolution-recrystallization processes likely occurred after RM was added. The dissolution and transformation of RM in Fe^{3+}-rich AMD resulted in a higher proportion of As immobilized in the precipitate. The decrease in the content of S observed was likely primarily due to partial dissolution of tooeleite and/or jarosites caused by the addition of alkaline RM, and partially due to weak ion-exchange reactions occurring between SO_4^{2-} and As(III) during the As immobilization process (Fig. S10). The XPS analysis detected higher contents of O and Si on the cell surfaces, indicating a formation of a SiO_2-gel (Fig. S11, Table S5), which has been postulated favorable for the stabilization of As-bearing precipitates (Adelman et al., 2015).

3.4.3. Evaluation of As immobilization mechanism

The above results indicate that RM greatly promoted the immobilization of dissolved As(III) released via arsenopyrite bio-oxidation, based on the much lower $[As(III)]_{aq}$ detected in AMD compared to BSM. There are two possible mechanisms for As(III) immobilization: (i) direct adsorption or co-precipitation of As(III); and (ii) initial oxidation of As(III) to As(V) and subsequent formation of As(V)-bearing precipitates. To determine the mechanism, the surface properties and the speciation of As and S of the precipitates after As(III) immobilization were investigated using FT-IR and As/S K-edge XANES.

The FT-IR spectra of all solid samples after RM additions (shown in Fig. S12)

exhibited the bands ascribed to O-H stretching (3,000-3,600 cm^{-1}) and H-O-H bending (1,627 cm^{-1}) vibrations of adsorbed water. The C-O-C band (1,400-1,500 cm^{-1}) corresponding to calcite was not detected in the spectrum of the solid sample collected from the AMD assay with 4 g/L RM, due to RM complete dissolution (Zhang et al., 2022; as opposed to partial RM dissolution in assays with 8 g/L RM). An increase in the intensity of bands ascribed to $v_1(AsO_3^{3-})$ (770 cm^{-1}) and $v_3(AsO_3^{3-})$ (the shoulder at 694 cm^{-1}) indicate that more As(III) was adsorbed onto the surface of the AMD precipitate after a 8 g/L RM addition, compared to the BSM precipitate. Three SO_4^{2-} bands (at 1,112, 985, and 603 cm^{-1}) corresponding to $v_3(SO_4)$, outer sphere bound $v_1(SO_4)$, and structural $v_4(SO_4)$ in tooeleite, respectively (Chai et al., 2016), were detected in all precipitates, and the intensities of these peaks in the solids collected from the AMD assays with RM were higher than in the precipitates from the BSM assay with RM.

The As K-edge XANES spectra (Fig. 13a) show that the intensity of the peak for As(III) (11,871.3 eV) increased significantly in the precipitates from the AMD assays after RM additions, while the peak for As(V) (11,875 eV) remained almost unchanged. A similar trend was observed in the precipitates from the BSM assay. The LCF results (Fig. 13b, c) indicate that the As species in the precipitate obtained from the BSM assay with 8 g/L RM were composed of 33.6% amorphous FA, 28.8% tooeleite, 23.2% Na_3AsO_3, and 14.4% scorodite. In the solids from the AMD assays, tooeleite dominated (with 70.4% and 73.1% in the assays with 4 and 8 g/L RM, respectively), followed by Na_3AsO_3 (18.8 and 20.6% respectively) and <10% amorphous FA. Compared to the

LCF results of the precipitates before RM additions, the proportion of the As(V)-bearing component (i.e., amorphous FA) decreased in the precipitates from both AMD assays (with 4 and 8 g/L RM) (Fig. 13c). Based on the above results, it can be concluded that no significant As oxidation occurred during RM dissolution and As(III) immobilization.

The results of S K-edge XANES show that compared to the spectrum of the residue from the BSM assay with 8 g/L RM, significantly lower intensities of the peak for S^0 (2,472.6 eV) and higher intensities of the peak for SO_4^{2-} (2,482.8 eV) were observed in the spectra of the residues obtained from AMD assays with both RM additions (Fig. 14a). The LCF results (Fig. 14b and Table 2) show that the content of jarosites decreased in all assays after RM additions, likely due to the increase in pH above the range within which jarosites are stable (approx. 1 to 2.5) and their subsequent transformation into schwertmannite (Bigham et al., 1996). The dissolution of aluminosilicates (e.g., kaolinite and katoite ($Ca_3Al_2(SiO_4)(OH)_8$), following Eqs. 7 and 8 respectively) and Ca-bearing phases (e.g., calcite; Eq. 9) releases Al^{3+} and Ca^{2+} into solution. These cations can react with SO_4^{2-} generated via S bio-oxidation, forming insoluble crystalline $Al_2(SO_4)_3$ and $CaSO_4$ (Eqs. 10 and 11 respectively). As shown in Table 2, the S compounds in the precipitate collected from the AMD assay four days after the addition of 4 g/L RM comprised 35.6% tooeleite, 27.4% $CaSO_4$, and 12.8% S^0, with minor amounts of schwertmannite (9.2%), $Al_2(SO_4)_3$ (8.9%), and jarosites (6.1%). The contents of S^0 and jarosites decreased to 6.3% and 0% respectively when a higher amount of RM (8 g/L) was added, while the contents of schwertmannite, tooeleite, and

$CaSO_4$ increased slightly (Table S6). Fig. S13 shows that RM alone promotes S^0 oxidation only marginally. These results demonstrate that RM promotes oxidation of S^0 and transformations of the secondary sulfate minerals.

$$Al_2Si_2O_5(OH)_4 + 6H^+ \rightarrow 2Al^{3+} + 2H_4SiO_4 + H_2O \quad (7)$$

$$Ca_3Al_2(SiO_4)(OH)_8 + 12H^+ \rightarrow 3Ca^{2+} + 2Al^{3+} + H_4SiO_4 + 8H_2O \quad (8)$$

$$CaCO_3 + 2H^+ \rightarrow Ca^{2+} + H_2O + CO_2 \quad (9)$$

$$2Al^{3+} + 3{SO_4}^{2-} \rightarrow Al_2(SO_4)_3 \quad (10)$$

$$Ca^{2+} + {SO_4}^{2-} \rightarrow CaSO_4 \quad (11)$$

It can be concluded that RM can promote immobilization of As(III) released via arsenopyrite bio-oxidation under acidic conditions (especially in AMD), through the regulation of $[Fe^{3+}]_{aq}$, pH, and ORP, and transformations of secondary products. No detectable oxidation of As(III) to As(V) was observed during the immobilization process, indicating that the compounds in RM do not mediate As oxidation. We speculate that there are three ways by which RM promotes As(III) immobilization: (1) the increase in solution pH caused by RM dissolution leads to a reduced stability of secondary sulfate minerals (e.g., jarosites and schwertmannite), and the unstable SO_4^{2-} groups contribute to As(III) immobilization via ligand exchange (supported by Figs. 9, 12 and Table S4); (2) RM provides nucleation sites for Fe^{3+} precipitation, thus promoting co-precipitation of As(III) as As(III)-Fe(III) oxyhydroxides such as tooeleite (shown in Figs. 13, 14) (Mamtaz and Bache, 2001; Meng et al., 2001); (3) the positively charged surface of RM that results from extensive Fe^{3+} and H^+ adsorption promotes the adsorption of As(III).

4. Conclusions

This study investigated the release and transport of As during bio-oxidation of arsenopyrite in natural AMD and compared the processes with those in BSM. Besides, the effects of an industrial solid waste (i.e., RM) on the immobilization of As(III) solubilized via arsenopyrite bio-oxidation were studied. The main findings are summarized below:

(1) The rate of bio-oxidation of arsenopyrite in AMD was higher than that in BSM, due to high concentrations of Fe^{3+} and SO_4^{2-} in AMD that enhanced arsenopyrite dissolution and As immobilization. Only 2.14% of arsenopyrite remained in the solid phase in the AMD biotic assay after 10 days of bio-oxidation, which was much less than in the BSM assay (10.56%).

(2) The attack of Fe^{3+} on arsenopyrite present in AMD generated elevated amounts of Fe^{2+}, which could serve as an electron donor promoting the growth of *S. thermosulfidooxidans*. Meanwhile, the bacterial cells served as nucleation sites for the precipitation of minerals. In contrast to jarosites dominating in BSM solids, tooeleite was the main secondary product in AMD residues.

(3) The As released via arsenopyrite bio-oxidation existed in solution as As(III). Importantly, $[As^T]_{aq}$ detected in AMD was significantly lower than in BSM. This was ascribed to the higher Fe(III)/As(III) ratio and $[SO_4^{2-}]$ in AMD favoring the formation of tooeleite and other secondary minerals (such as schwertmannite), which could significantly contribute to As immobilization.

(4) RM can effectively promote in-situ immobilization of As(III) released via

arsenopyrite bio-oxidation. The $[As(III)]_{aq}$ in the AMD assay decreased from 1.92 to 0.16 g/L after 4 days of reaction, which was a much lower value than that detected in BSM (1.43 g/L). The mechanism of As(III) immobilization using alkaline RM includes a ligand exchange with SO_4^{2-} in sulfate minerals affected by elevated pH, co-precipitation with Fe(III) on the RM surface, and direct adsorption of As(III) to the RM surface positively charged after Fe^{3+} adsorption. No oxidation of As(III) to As(V) was detected during As immobilization.

The results of this work provide a better understanding of the processes involved in bio-oxidation of arsenopyrite on contact with AMD and the fate of the immobilized As. The findings may contribute to the development of cost-effective technologies for the immobilization of As in mine wastes and mine-impacted environments.

Declaration of competing interest

The authors declare that they have no known competing financial interests or personal relationships that could have appeared to influence the work reported in this paper.

Acknowledgements

This work was supported by the financial support from the National Key Research and Development Program of China (2018YFE0110200), the Key Research and Development Program of Hunan Province, China (2020SK2125, 2022NK2057).

References

Adelman, J.G., Elouatik, S., Demopoulos, G.P., 2015. Investigation of sodium silicate-derived gels as encapsulants for hazardous materials - The case of scorodite. J. Hazard. Mater. 292, 108-117.

Adra, A., Morin, G., Ona-Nguema, G., Brest, J., 2016. Arsenate and arsenite adsorption onto Al-containing ferrihydrites. Implications for arsenic immobilization after neutralization of acid mine drainage. Appl. Geochem. 64, 2-9.

Bao, Y.P., Guo, C.L., Lu, G.N., Yi, X.Y., Wang, H., Dang, Z., 2018. Role of microbial activity in Fe(III) hydroxysulfate mineral transformations in an acid mine drainage-impacted site from the Dabaoshan Mine. Sci. Total. Environ. 616-617, 647-657.

Bigham, J.M., Schwertmann, U., Traina, S.J., Winland, R.L., Wolf, M., 1996. Schwertmannite and the chemical modeling of iron in acid sulfate waters. Geochim. Cosmochim. Acta. 60, 2111-2121.

Bond, P. L., Smriga, S. P., Banfield, J. F., 2000. Phylogeny of microorganisms populating a thick, subaerial, predominantly lithotrophic biofilm at an extreme acid mine drainage site. Appl. Environ. Microbiol. 66, 3842-3849.

Boussouga, Y.A., Mohankumar, M.B., Gopalakrishnan, A., Welle, A., Schäfer, A.I., 2021. Removal of arsenic(III) via nanofiltration: contribution of organic matter interactions. Water Res. 201, 117315.

Burton, E. D., Bush, R. T., Johnston, S. G., Watling, K. M., Hocking, R. K., Sullivan, L. A., Parker, G.K., 2009. Sorption of arsenic(V) and arsenic(III) to schwertmannite. Environ. Sci. Technol. 43, 9202-9217.

Chai, L., Yue, M., Yang, J., Wang, Q., Li, Q., Liu, H., 2016. Formation of tooeleite and the role of direct removal of As (III) from high-arsenic acid wastewater. J. Hazard. Mater. 320, 620-627.

Chen, M., Lu, G., Guo, C., Yang, C., Wu, J., Huang, W., Yee, N., Dang, Z., 2015. Sulfate migration in a river affected by acid mine drainage from the Dabaoshan mining area, South China. Chemosphere 119, 734-743.

Cheng, H., Hu, Y., Luo, J., Xu, B., Zhao, J., 2009. Geochemical processes controlling fate and transport of arsenic in acid mine drainage (AMD) and natural systems. J. Hazard. Mater. 165, 13-26.

Corkhill, C.L., Vaughan, D.J., 2009. Arsenopyrite oxidation-A review. Appl. Geochem. 24, 2342-2361.

Corkhill, C.L., Wincott, P.L., Lloyd, J.R., Vaughan, D.J., 2008. The oxidative dissolution of arsenopyrite (FeAsS) and enargite (Cu_3AsS_4) by *Leptospirillum ferrooxidans*. Geochim. Cosmochim. Acta 72, 5616-5633.

Datta, S., Rule, A.M., Mihalic, J.N., Chillrud, S.N., Bostick, B.C., Ramos-Bonilla, J.P., Han, I., Polyak, L.M., Geyh, A.S., Breysse, P.N., 2012. Use of X-ray absorption spectroscopy to speciate manganese in airborne particulate matter from five counties across the United States. Environ. Sci. Technol. 46, 3101-3109.

Duquesne, K., Lebrun, S., Casiot, C., Bruneel,O., Personne, J.C., Leblanc, M., Elbaz-Poulichet, F., Morin, G., Bonnefoy,V., 2003. Immobilization of arsenite and ferric iron by *Acidithiobacillus ferrooxidans* and its relevance to acid mine drainage. Appl. Environ. Microbiol. 69, 6165-6173.

Fandrich, R., Gu, Y., Burrows, D., Moeller, K., 2007. Modern SEM-based mineral liberation analysis. Int. J. Miner. Process. 84, 310-320.

Guo, H., Ren, Y., Liu, Q., Zhao, K., Li, Y., 2013. Enhancement of arsenic adsorption during mineral transformation from siderite to goethite: mechanism and application. Environ. Sci. Technol. 47, 1009-1016.

Hong, J., Liu, L.H., Ning, Z.P., Liu, C.S, Qiu, G.H., 2021. Synergistic oxidation of dissolved As(III) and arsenopyrite in the presence of oxygen: formation and function of reactive oxygen species. Water Res. 202, 117416.

Igarashi, T., Herrera, P.S., Uchiyama, H., Miyamae, H., Iyatomi, N., Hashimoto, K., Tabelin, C.B., 2020. The two-step neutralization ferrite-formation process for sustainable acid mine drainage treatment: removal of copper, zinc and arsenic, and the influence of coexisting ions on ferritization. Sci. Total Environ. 715, 136877.

Karamanev, D.G., Nikolov, L.N., Mamatarkova, V., 2002. Rapid simultaneous quantitative determination of ferric and ferrous ions in drainage. Miner. Eng. 15, 341-346.

Koo, T.H., Kim, J.W., Park, K.R., 2022. Formation of pharmacosiderite ($KFe_4(AsO_4)_3(OH)_4 \cdot 6\text{-}7H_2O$) in the acid-sulfate-chloride (ASC) geothermal spring, Norris Geyser Basin, Yellowstone National Park, USA: Implication of Fe and As redox reaction associated with microbe and clay minerals. Appl. Clay Sci. 216, 106343.

Larsson, L., Olsson, G., Holst, O., Karlsson, H., 1990. Pyrite oxidation by thermophilic archaebacteria. Appl. Environ. Microbiol. 56, 697-701.

Liu, Z., Lei, H.Y., Bai, T., Wang, W.Z., Chen, K., Chen, J.J., Hu, Q.W., 2015.

Microwave-assisted arsenic removal and the magnetic effects of typical arsenopyrite-bearing mine tailings. Chem. Eng. J. 272, 1-11.

Ma, Y.Q., Qin, Y.W, Zheng, B.H., Zhang, L., Zhao, Y.M., 2016. Arsenic release from the abiotic oxidation of arsenopyrite under the impact of waterborne H_2O_2: a SEM and XPS study. Environ. Sci. Pollu. Res. 23, 1381-1390.

Mamtaz, R., Bache, D.H., 2001. Reduction of arsenic in groundwater by coprecipitation with iron. J. Water Supply Res. Technol. 50, 313-324.

Egal, M., Casiot, C., Morin, G., Parmentier, M., Bruneel, O., Lebrun, S., Elbaz-Poulichet F., 2009. Kinetic control on the formation of tooeleite, schwertmannite and jarosite by *Acidithiobacillus ferrooxidans* strains in an As(III)-rich acid mine water. Chem. Geol. 265, 432-441.

Matschullat, J., 2000. Arsenic in the geosphere-a review. Sci. Total Environ. 249, 297-312.

McKibben, M.A., Tallant, B.A., del Angel, J.K., 2008. Kinetics of inorganic arsenopyrite oxidation in acidic aqueous solutions. Appl. Geochem. 23, 121-135.

Meng, X.G., Korfiatis, G.P., Christodoulatos, C., Bang, S.B., 2001. Treatment of arsenic in Bangladesh well water using a household co-precipitation and filtration system. Water Res. 35, 2805-2819.

Morin, G., Juillot, F., Casiot, C., Bruneel, O., Personné, J., Elbaz-Poulichet, F., Leblace, M., Iidefonse, P., Calas, G., 2003. Bacterial formation of tooeleite and mixed arsenic(III) or arsenic(VI)-Iron(III) gels in the Carnoulès acid mine drainage, France. A XANES, XRD, and SEM study. Environ. Sci. Technol. 37, 1705-1712.

Murciego, A., Alvarez-Ayuso, E., Aldana-Martínez, S.C., Sanz-Arranz, A., Medina-García, J., Rull-Perez, F., Villar-Alonso, P., 2019. Characterization of secondary products in arsenopyrite-bearing mine wastes: influence of cementation on arsenic attenuation. J. Hazard. Mater. 373, 425-436.

Neil, C.W., Jun, Y.S., 2016. Fe^{3+} Addition Promotes Arsenopyrite Dissolution and Iron (III)(Hydr) oxide Formation and Phase Transformation. Environ. Sci. Technol. Lett. 3, 30-35.

Nishimura, T., Robins, R.G., 2008. Confirmation that tooeleite is a ferric arsenite sulfate hydrate, and is relevant to arsenic stabilization. Miner. Eng. 21, 246-251.

Park, I., Higuchi, K., Tabelin, C. B., Jeon, S., Hiroyoshi, N., 2020. Suppression of arsenopyrite oxidation by microencapsulation using ferric-catecholate complexes and phosphate. Chemosphere 269, 129413.

Park, I., Tabelin, C.B., Jeon, S., Li, X., Seno, K., Ito, M., Hiroyoshi, N., 2019. A review of recent strategies for acid mine drainage prevention and mine tailings recycling. Chemosphere 219, 588-606.

Ravel, B., Newville, M., 2005. ATHENA, ARTEMIS, HEPHAESTUS: data analysis for X-ray absorption spectroscopy using IFEFFIT. J. Synchrotron Radiat. 12, 537-541.

Savage, K.S., Bird, D.K., O'Day, P.A., 2005. Arsenic speciation in synthetic jarosite. Chem. Geol. 215, 473-498.

Tabelin, C.B., Park, I., Phengsaart, T., Jeon, S., Villacorte-Tabelin, M., Alonzo, D., Yoo, K., Ito, M., Hiroyoshi, N., 2021. Copper and critical metals production from porphyry ores and E-wastes: a review of resource availability, processing/recycling challenges,

socio-environmental aspects, and sustainability issues. Resour. Conserv. Recycl. 170, 105610.

Vega-Hernandez, S., Weijma, J., Buisman, C.J.N., 2019. Immobilization of arsenic as scorodite by a thermoacidophilic mixed culture via As(III)-catalyzed oxidation with activated carbon. J. Hazard. Mater. 368, 221-227.

Walker, F.P., Schreiber, M.E., Rimstidt, J.D., 2006. Kinetics of arsenopyrite oxidative dissolution by oxygen. Geochim. Cosmochim. Acta. 70, 1668-1676.

Wang, X.M., Jiang, H.K., Fang, D., Liang, J.R., Zhou, L.X., 2019. A novel approach to rapidly purify acid mine drainage through chemically forming schwertmannite followed by lime neutralization. Water Res. 151, 515-522.

Wang, X., Li, Q.Z., Liao, Q., Yan, Y.C., Xia, J., Lin, Q.H., 2020. Arsenic(III) biotransformation to tooeleite associated with the oxidation of Fe(II) via *Acidithiobacillus ferrooxidans*. Chemosphere 248, 126080.

Wei, Y.F., Liu, H., Liu, C.B., Luo, S.L., Liu, Y.T., Yu, X.W., Ma, J.H., Yin, K., Feng, H.P., 2019. Fast and efficient removal of As(III) from water by $CuFe_2O_4$ with peroxymonosulfate: Effects of oxidation and adsorption. Water Res. 150, 182-190.

Wu, X.，Bowers, B., Kim, D., Lee, B., Jun, Y.S., 2019. Dissolved Organic Matter Affects Arsenic Mobility and Iron(III) (hydr)oxide Formation: Implications for Managed Aquifer Recharge. Environ. Sci. Technol. 53, 14357-14367.

Wu, X., Burnell, S., Neil, C.W., Kim, D., Zhang, L., Jung, H., Jun, Y., 2020b. Effects of phosphate, silicate, and bicarbonate on arsenopyrite dissolution and secondary mineral precipitation. ACS Earth Space Chem. 4, 515-525.

Yu, Y., Zhu, Y., Gao, Z., Gammons, C.H., Li, D., 2007. Rates of Arsenopyrite Oxidation by Oxygen and Fe (III) at pH 1.8-12.6 and 15-45° C. Environ. Sci. Technol. 41, 6460-6464.

Yuan, Z.D., Ma, X., Wang, S.F., Yu, L., Zhang, P.W., Liu, J.R., Jia, Y.F., 2021. Effect of co-existent Al(III) in As-rich Acid Mine Drainage (AMD) on As removal during Fe(II) and As(III) abiotic oxidation process. J. Water Process. Eng. 44, 102395.

Zhang, D.R., Chen, H.R., Zhao, X.J., Xia, J.L., Nie, Z.Y., Zhang, R.Y., Shu, W.S., Pakostova, E., 2022. Fe(II) bio-oxidation mediates red mud transformations to form Fe(III)/Al (hydr)oxide adsorbent for efficient As(V) removal under acidic conditions. Chem. Eng. J. 439, 13573.

Zhang, D.R., Chen, H.R., Xia, J.L., Nie, Z.Y., Fan, X.L., Liu, H.C., Zheng, L., Zhang, L.J., Yang, H.Y., 2020. Humic acid promotes arsenopyrite bio-oxidation and arsenic immobilization. J. Hazard Mater. 384, 121359.

Zhang, D.R., Chen, H.R., Xia, J.L., Nie, Z.Y., Zhang, R.Y., Schippers, A., Shu, W.S., Qian, L.X., 2021. Red mud regulates arsenic fate at acidic pH via regulating arsenopyrite bio-oxidation and S, Fe, Al, Si speciation transformation. Water Res. 203, 117539.

Zhang, G., Chao, X., Guo, P., Cao, J., Yang, C., 2015. Catalytic effect of Ag+ on arsenic bioleaching from orpiment (As_2S_3) in batch tests with *Acidithiobacillus ferrooxidans* and *Sulfobacillus sibiricus*. J. Hazard. Mater. 283, 117-122.

Zheng, K., Li, H., Wang, S., Feng, X.N., Wang, L.Y., Liu, Q.Y., 2020. Arsenopyrite weathering in sodium chloride solution: Arsenic geochemical evolution and

environmental effects. J. Hazard. Mater. 392, 122502.

Table 1. Elemental composition of and Fe/As ratio (determined by TEM-EDS) in the surface structures of the precipitates collected from the biotic AMD system before (on day 10) (a) and after (on day 14) (b) the addition of 8 g/L RM.

Commented [LS1]: Correct?

Sample	Element (%)								Fe/As
	O	Fe	As	S	Al	Si	Ca	K	
a	52.29	26.13	16.54	4.83	0.12	0.04	0.03	0.02	1.57
b	64.68	12.78	8.77	3	3.54	7.08	0.09	0.06	1.46

Table 2. LCF results for the S K-edge XANES spectra of the precipitates obtained from the AMD assays with 4 (AMD-4) and 8 g/L (AMD-8) RM, and from the 0K medium with 8 g/L RM (0K-8). Legend: Jaro = jarosite, Sch = schwertmannite.

Sample	Proportion of sulfur-bearing compounds (%)							
	FeAsS	S^0	Jaro	Sch	tooeleite	$Al_2(SO_4)_3$	$CaSO_4$	R-factor
AMD-4	-	12.8	6.1	9.2	35.6	8.9	27.4	0.0009
AMD-8	-	6.3	0	11.5	40.5	7.4	34.3	0.0004
0K-8	6.8	36.1	15.6	5.5	16.3		19.7	0.0006

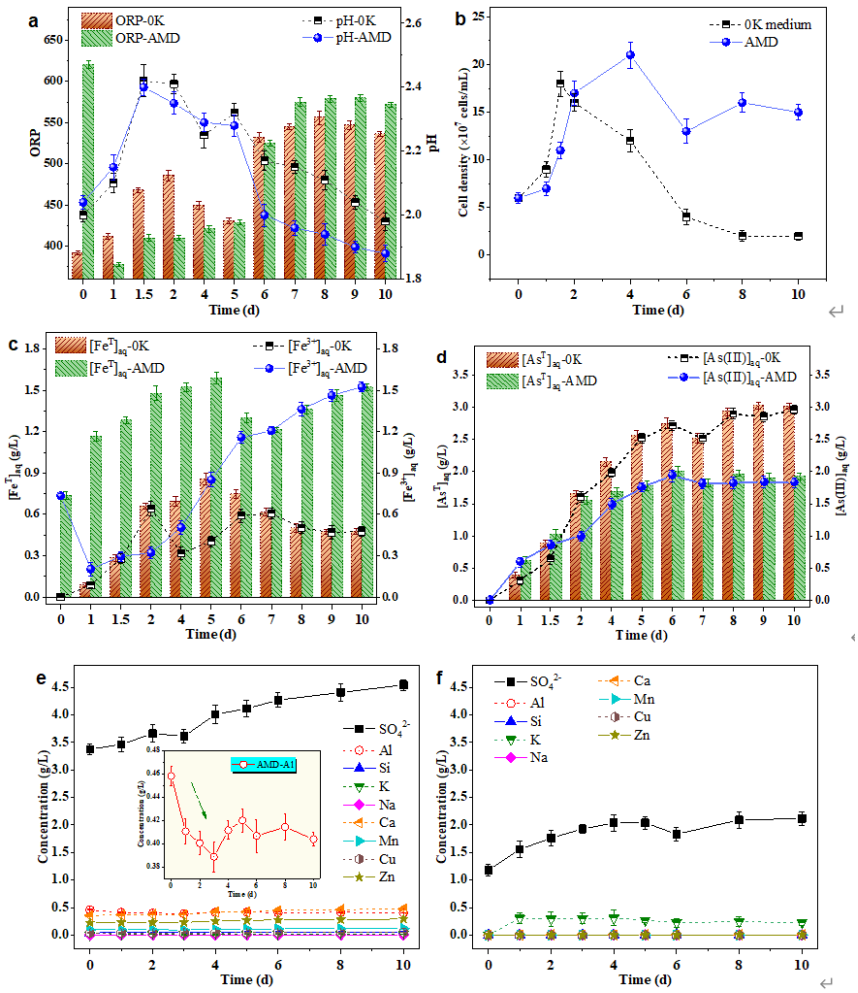

Fig. 1. Solution parameters during arsenopyrite bio-oxidation by *S. thermosulfidooxidans* in AMD water and BSM. Changes in (a) ORP and pH, (b) cell density, (c) $[Fe^T]_{aq}$ and $[Fe^{3+}]_{aq}$, (d) $[As^T]_{aq}$ and $[As(III)]_{aq}$, (e) concentrations of SO_4^{2-} and other elements in AMD water, (f) concentrations of SO_4^{2-} and other elements in BSM.

Commented [LS2]: The unit of ORP (mV) is missing in the chart axis label.

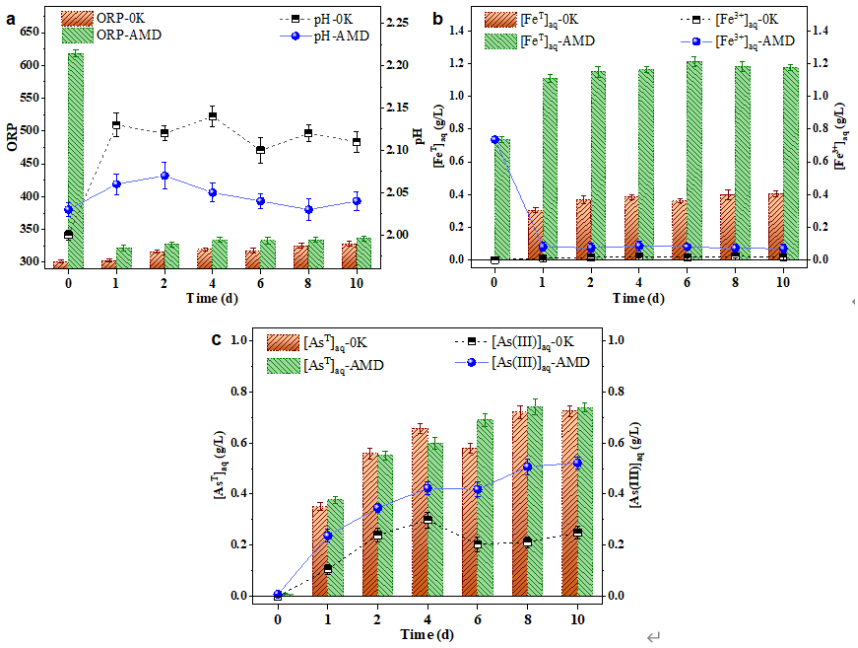

Fig. 2. Solution parameters in sterile controls showing abiotic dissolution of arsenopyrite in AMD water and BSM. Changes in (a) ORP and pH, (b) $[Fe^T]_{aq}$ and $[Fe^{3+}]_{aq}$, (c) $[As^T]_{aq}$ and $[As(III)]_{aq}$.

Commented [LS3]: The ORP unit (mV) is again missing in the axis label in the chart.

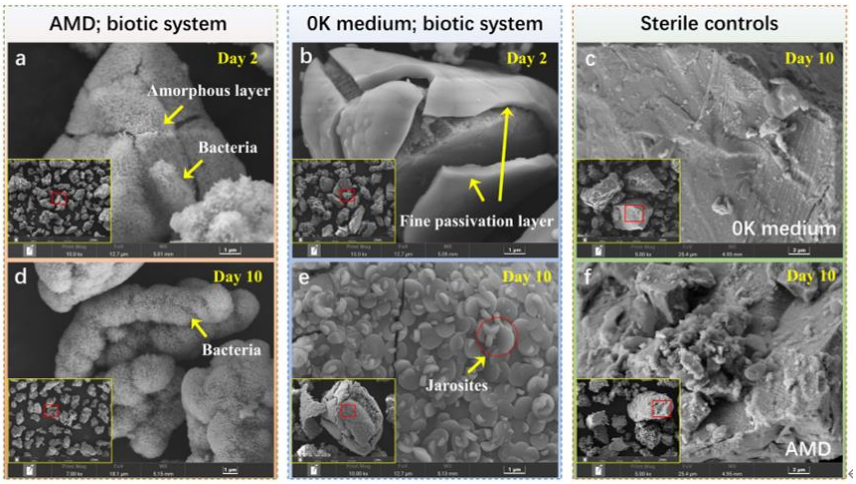

Fig. 3. SEM images of arsenopyrite residues and precipitates collected from AMD (a, d) and BSM (b, e) biotic assays after 2 (a, b) and 10 (d, e) days of arsenopyrite bio-oxidation; SEM images of solids collected from BSM (c) and AMD (f) sterile controls after 10 days.

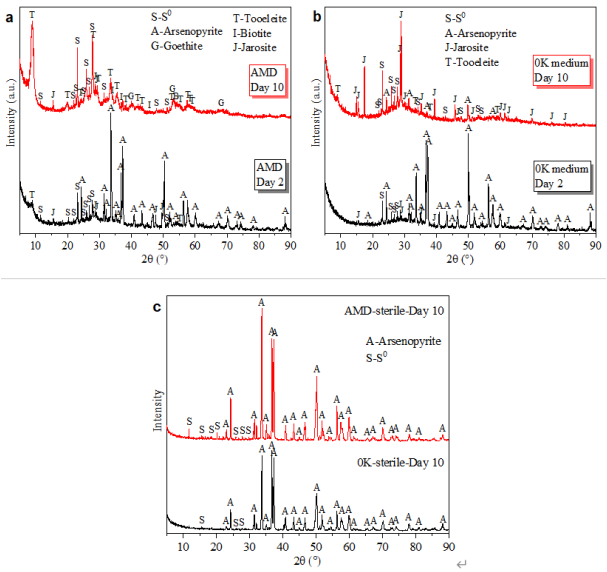

Fig. 4. XRD patterns of solids after 2 and 10 days of arsenopyrite bio-oxidation in AMD (a) and BSM (b), and in sterile controls after 10 days (c).

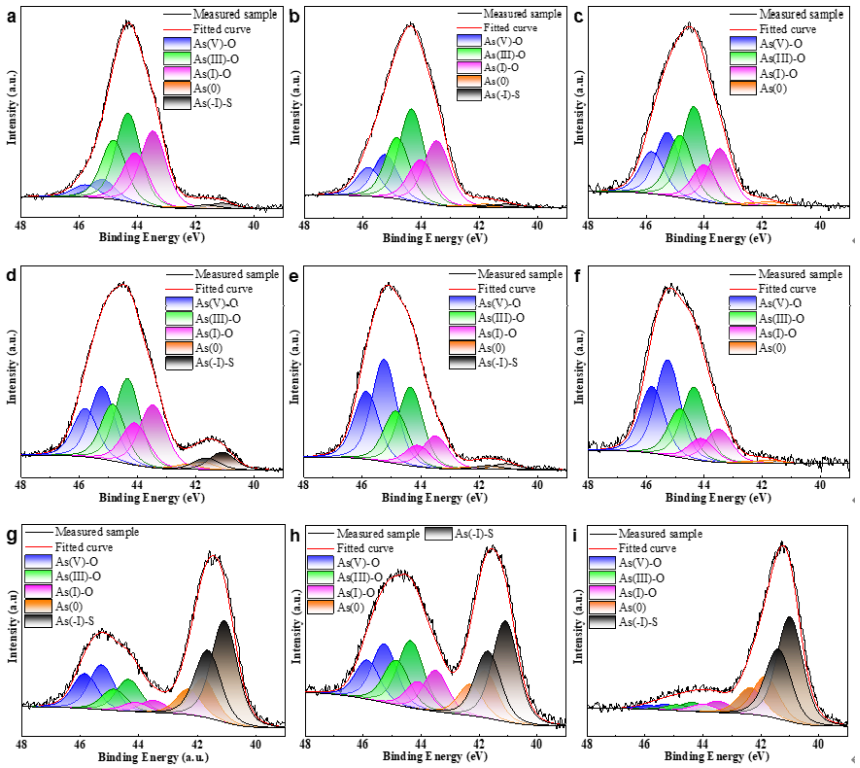

Fig. 5. XPS spectra of the oxidation layers on the surface of arsenopyrite bio-oxidized in AMD for 2 (a), 4 (b), and 10 (c) days, and in the BSM for 2 (d), 4 (e), and 10 (f) days; XPS spectra of the residues collected from AMD (g) and BSM (h) sterile controls after 10 days; spectrum of the original arsenopyrite (i).

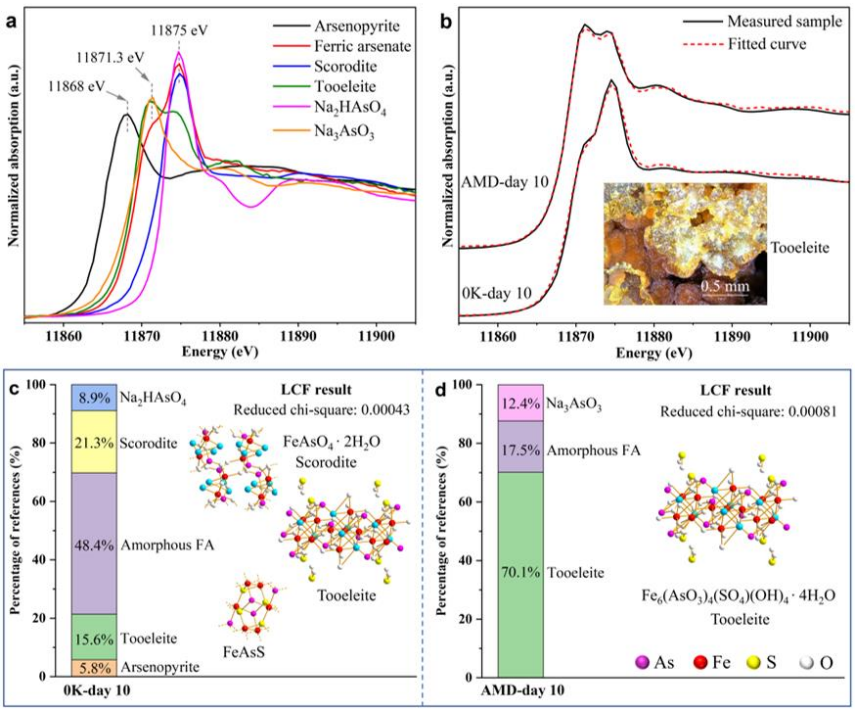

Fig. 6. (a) As K-edge XANES spectra of As-bearing references; (b) XANES spectra of solid samples after arsenopyrite bio-oxidation for 10 days in AMD and BSM (black solid lines), and the LCF results (red dot lines) fitted using the above references; (c, d) proportions of As-bearing compounds in spectra of solid samples collected from the BSM and AMD assays, respectively. Legend: FA = ferric arsenate.

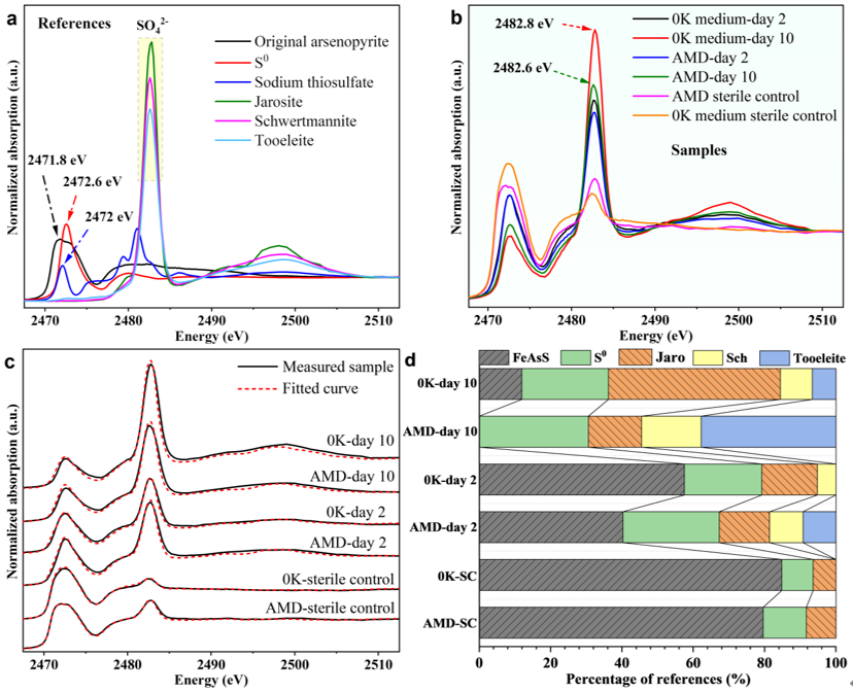

Fig. 7. (a) S K-edge XANES spectra of S-bearing references; (b) XANES spectra of solids collected from the biotic systems after 2 and 10 days of arsenopyrite bio-oxidation and from sterile controls after 10 days; (c) LCF results; (d) proportions of S-bearing compounds in spectra of solid samples analyzed. Legend: Jaro = jarosite, Sch = schwertmannite.

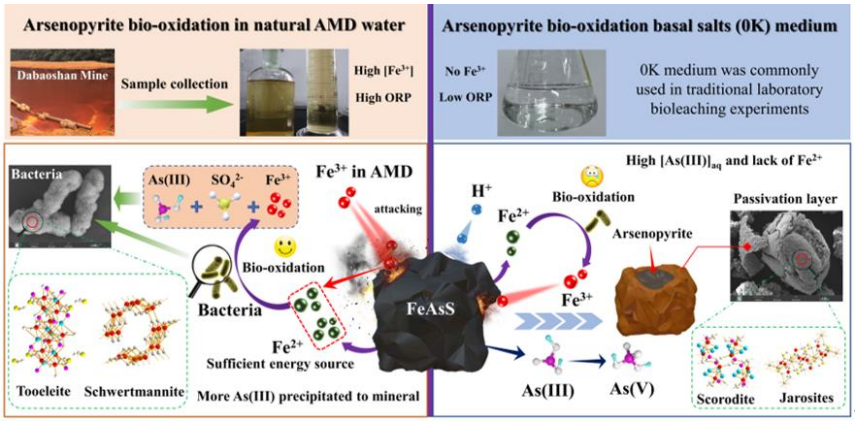

Fig. 8. Schematic diagram of arsenopyrite bio-oxidation and As speciation transformations in AMD (left) and BSM (right).

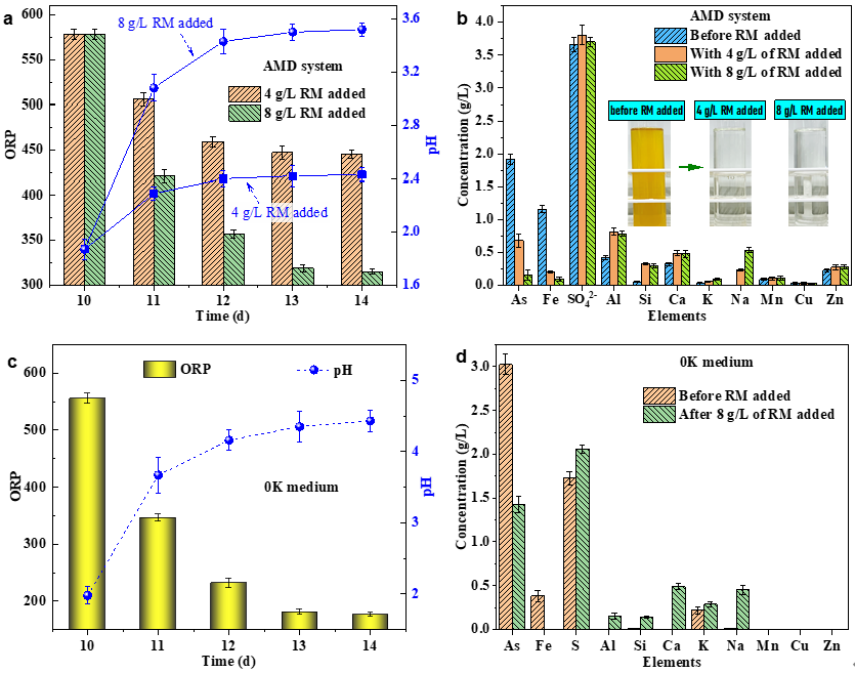

Fig. 9. Changes in (a, c) ORP and pH values, and (b, d) the concentrations of dissolved elements in the AMD (upper row) and BSM (bottom row) biotic systems after RM additions on day 10.

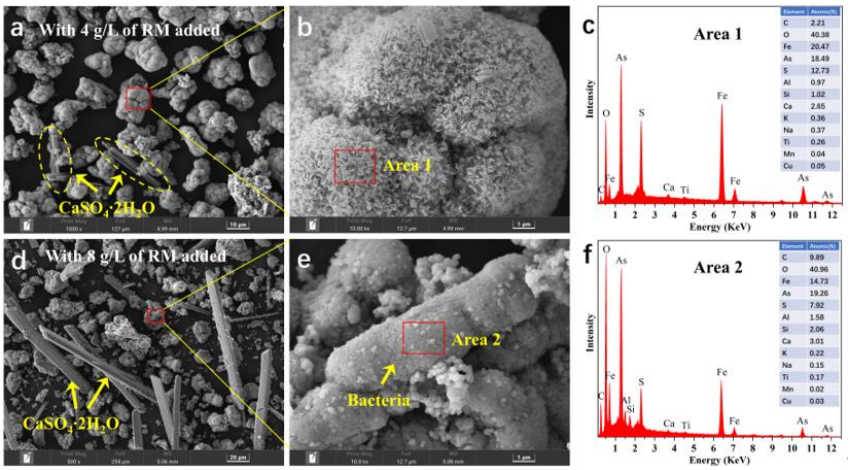

Fig. 10. SEM images of precipitates collected from AMD biotic systems four days after 4 (a, b) and 8 g/L (d, e) of RM were added to the arsenopyrite bio-oxidation assays on day 10; (c, f) EDS results for the areas marked in Fig. 10b and e respectively.

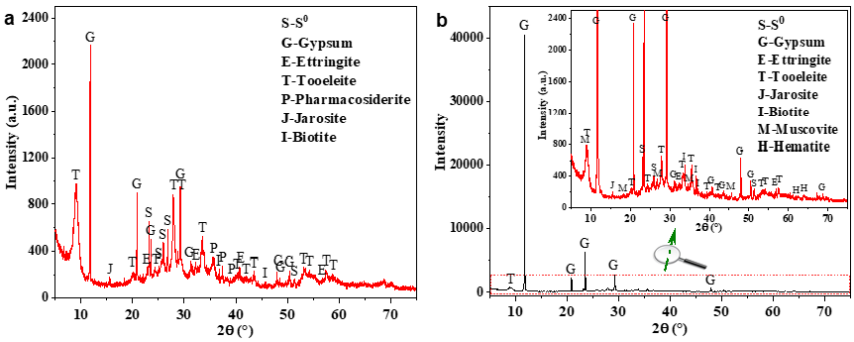

Fig. 11. XRD patterns of the precipitates collected four days (i.e., on day 14) after the additions of 4 (a) and 8 g/L (b) of RM to the arsenopyrite bio-oxidation assays.

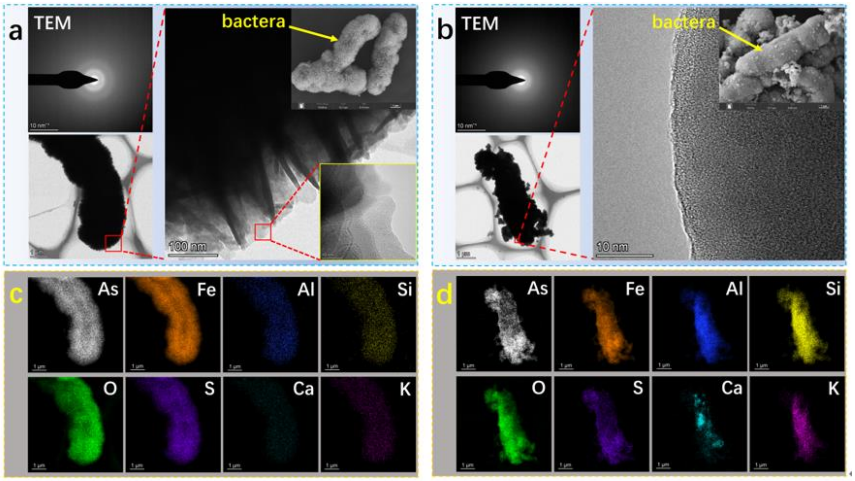

Fig. 12. TEM and HRTEM images (a, b), and elemental mapping (c, d) of the precipitates collected from the AMD biotic system before (on day 10) (a, c) and after (on day 14) (b, d) the addition of 8 g/L RM.

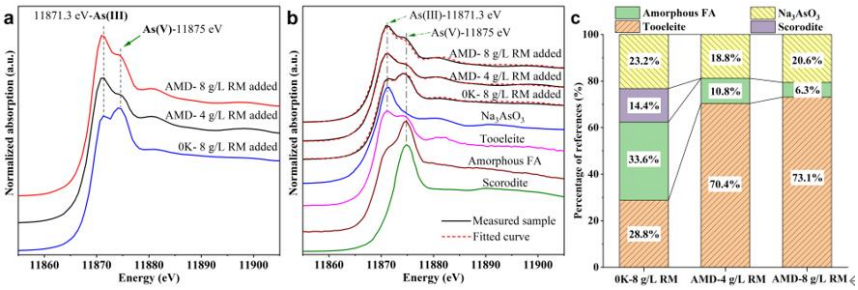

Fig. 13. (a) As K-edge XANES spectra of precipitates after As(III) immobilization by RM; (b) LCF results for the precipitates, using the As-bearing references shown; (c) proportions of As-bearing compounds in the solid samples. Legend: FA = ferric arsenate.

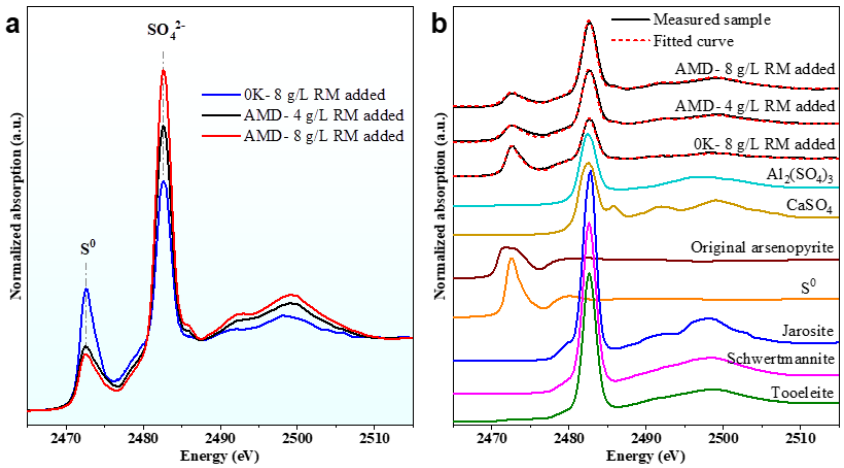

Fig. 14. (a) S K-edge XANES spectra of the precipitates collected from the biotic assays after As(III) immobilization by RM; (b) LCF results for the precipitates, determined using the references shown.